The Laser System of Very Compact Inverse Compton Scattering γ-ray Source at Tsinghua university*

Qi-li Tian,[1,2] Qiang Gao,[1,2] Xing Liu,[1,2] Xin-yi Lu,[1,2] Huan Wang,[1,2] Ze-xin Song,[1,2] Jing-jing You,[1,2] Zhi-jun Chi,[3] Li-xin Yan,[1,2,†] Ying-chao Du,[1,2] Jia-ru Shi,[1,2] Ren-kai Li,[1,2] Wen-hui Huang,[1,2] and Chuan-xiang Tang[1,2]

[1]*Department of Engineering Physics, Tsinghua University, Beijing 100084, China*
[2]*Key Laboratory of Particle and Radiation Imaging of Ministry of Education, Department of Engineering Physics, Tsinghua University, Beijing, China*
[3]*Key Laboratory of Beam Technology of Ministry of Education, School of Physics and Astronomy, Beijing Normal University, Beijing 100875, China*

With the development of high-brightness electron beams and chirped pulse amplification technology, the inverse Compton scattering (ICS) X/γ-ray have the characteristics of compactness, quasi-monochromatic, continuous energy tunability, and high photon energy. The application of ultra-fast laser technology has improved the temporal resolution, brightness, and spectral control capabilities of the X/γ-ray. In this paper, we present the design and implementation of the laser system for the very compact inverse Compton scattering γ-ray source (VIGAS). The laser system consists of a photo-injector driving laser system and a scattering laser system. The photo injector driving laser system produces an ultraviolet (UV) pulses with 0.58 mJ pulse energy, 7.2 ps (FWHM) pulse width, and 10 Hz repetition rate at a central wavelength of 267 nm, which illuminates a photocathode to generate a high-quality electron beam. The ICS laser system produces two alternative ultra-short laser pulses with a central wavelength of 800 nm and 400 nm, respectively, to interact with the electron beam. An intense second harmonic (SH) laser with 0.5 J pulse energy is achieved experimentally by passing a TW Ti:sapphire laser pulse through a 0.59-mm KDP crystal. We obtain a uniform SH laser focal intensity distribution through wavefront correction by a deformable mirror.

Keywords: Inverse Compton scattering γ-ray, Photo injector drive laser, Second harmonic generation, Wave front correction

I. INTRODUCTION

High brightness X/γ-ray source based on the ICS interaction between high-energy electron beams and intense laser pulses supplies a powerful tool for exploring the microstructure of matter and promoting the development of fundamental research[1–3].The advanced X-ray imaging techniques based on ICS light source, e.g. K-edge subtraction imaging[4], phase-contrast imaging[5, 6], and X-ray fluorescence computed tomography[7, 8], lead the development of medical imaging methods and have been proven to have advantages over conventional X-ray imaging methods in disease diagnosis. Driven by the important applications and remarkable advancements of the high brightness electron source and high power laser techniques, high photon-energy quasi-monochromatic X/γ-ray sources have been developed or developing around the world at many labs, such as the SPARC LAB Thomson source[9], ThomX in LAL Laboratory[10], ELI-NP in Romania[11], NewSUBARU in Japan[12], MEGa-ray source in LLNL[13], SLEGS in SINAP[14–16], LCS-gamma ray source in IHEP[17], XGLS in Xi'an[18] and TTX in Tsinghua university[19, 20]. The VIGAS facility would probably be the first compact ICS γ-ray source with photon energy up to the MeV level, which could be continuously adjustable between 0.2-4.8 MeV[21]. The source will be applied in researches such as advanced imaging, nuclear resonant fluorescence, etc.

As the key components of ICS X/γ-ray sources, the laser systems are critical for the performance of an ICS light source[22–24]. A high-quality electron source with low beam emittance is crucially determined by the spatial and temporal profile of the UV driving laser pulses[25–27]. In the ICS process, the impact of the scattering laser parameters on the characteristics of X/γ-ray is primarily including the following aspect[28]: a) The X/γ-ray photon energy is proportional to the photon energy of the scattering laser; b) The photon yield is directly proportional to the laser pulse energy; c) The photon yield is also related to the pulse duration and focal size of the scattering laser; d) The polarization and spectrum of X/γ-ray depends on the laser polarization and spectrum, respectively; e) The stability of the X/γ-ray will be affected by the pointing stability of the scattering laser pulse.

In this paper, we will report the design implementation, and experimental data of the laser system for the VIGAS facility, including the engineering modular layouts of photo-injector UV driving and ICS lasers. A UV laser with 2 mJ pulse energy at 267 nm was generated with third harmonic generation (THG) conversion efficiency 24% and then spatially and temporally shaped for the generation of electron beams. The shaped UV laser was used to simulate the election beam characteristics by GPT, leading to a normalized rms emittance of 0.6 mm.mrad at a charge of 200 pC. Moreover, we have experimentally studied the second harmonic generation (SHG) of ultrahigh intensity femtosecond laser pulses in KDP crystal. A 400 nm laser pulse with 0.5 J pulse energy was generated for the production of higher photon-energy γ-ray.

* Supported by the National Natural Science Foundation of China (Nos.12027902,12375157). We thank QiFeng New Light Source Co., Ltd for help with the ICS laser system.

† Li-xin Yan, yanlx@mail.tsinghua.edu.cn, Department of Engineering Physics, Tsinghua University, Beijing 100084, China.

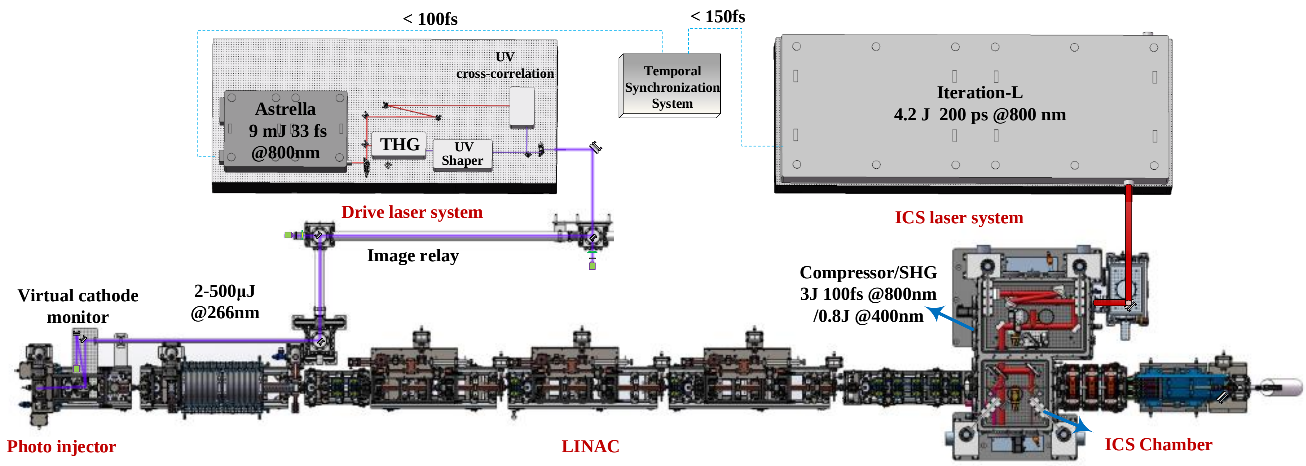

Fig. 1. The Laser system layout of the VIGAS facility Schematic.

II. LASER SYSTEMS DESIGN OF THE VIGAS

Table 1. Parameters of the laser system.

Laser parameters	Driving laser	ICS laser
Central wavelength/nm	267	800 /400
Repetition rate/Hz	10	10
Pulse energy	2$\sim$500 μJ	$\geq$ 1.5 J@800 nm/ $\geq$ 0.8 J@400 nm
Energy jitter(RMS)/%	$<$ 1.0	$<$ 1.2
Pulse width(FWHM)/ps	5$\sim$10	0.1$\sim$10
Beam size	0.2$\sim$2 mm[a]	$<$ 10 μm(RMS)
Beam pointing stability/μrad	$<$ 10	$<$ 2
Time jitter(RMS)/fs	$<$ 100	$<$ 150

[a] The driving laser is formed by transversly truncating a Gaussian beam with a hard-edge iris. Beam size is in diameter.

The requirements of VIGAS for the laser parameters are shown in Table 1. Since the material of the photocathode is copper, the wavelength of the driving laser is in the ultraviolet range, with a central wavelength of 267 nm. By adjusting the energy of the driving laser within the range of 2-500 μJ, we can continuously control the charge of electron beam. The spatial and temporal distribution of the driving laser significantly impacts the beam emittance. Typically, the initial laser distribution follows a Gaussian shape, and to achieve low beam emittance, shaping the spatial-temporal distribution into a flat-top profile is necessary. According to beam simulation calculations, the driving laser pulse width ranges from 5 to 10 ps, with a transverse size of 0.2 to 2 mm. In the VIGAS project, the ICS laser requires two wavelengths of 800 nm and 400 nm, with corresponding pulse energies of 1.5 J and 0.8 J, to generate γ-rays with different photon energies. To increase photon yield, the focal spot size of the ICS laser needs to be less than 10 μm (RMS), and its pointing stability < 2 μrad.

The schematic design of VIGAS laser systems is shown in Fig.1. Both lasers are commercial Ti: sapphire laser with a central wavelength of 800 nm and operate at a repetition rate of 10 Hz. The drive laser is an Astrella ultrafast amplifier laser system from Coherent, Inc. The UV laser for the photocathode RF gun is generated via a THG process, UV energy tuner, spatial-temporal shaping and image relay modules. The ICS laser is an Iteration-TW high energy commercial laser amplifier from Qifeng new light source, Inc. After transportation through a pulse compressor, a laser parameter adjust and control system, and a laser focusing unit, the ICS laser generates an intense focal spot at the interaction point (IP) for scattering with the electron beams.

The electron beam is initiated by the UV photocathode laser and then accelerated by a combined S-band[29] and X-band[30, 31] linac to 50-350 MeV beam energy. The beam makes a head-on collision with the tightly focused ICS laser for γ-ray generation. The two laser systems are phase-locked to a 2856 MHz master clock signal with a time jitter of less than 100 fs and 150 fs, respectively.

The UV photoinjector driving laser system adopts an engineering modular design. Figure 2(a)-(b) illustrates the optical design schematics and assembled setup of the UV THG converter, respectively. The SH laser is generated by the β-BBO1 crystal (CASTECH; size 20 mm$\times$ 20 mm, 0.3 mm-thickness, $\theta = 29.2°$) and then separated from the fundamental laser (800 nm) using a dichroic mirror (DM1). The polarization of the fundamental laser is rotated by 90∘ using a half-wave plate, and after a time delay, it overlaps with the SH laser in the sum-frequency crystal (β-BBO2, size 20 mm$\times$ 20 mm, 0.3 mm-thickness, $\theta = 44.3°$) for THG. The THG laser is separated using two dichroic mirrors and then transmitted to the UV spatial-temporal shaping module. The UV energy tuner and pulse shaper are integrated into one module, as shown in Fig. 2(c)-(d). The UV energy tuner consists of a half-wave plate and a Glan laser polarizer. By tuning the incident UV laser energy on the photocathode gun, the beam charge can be controlled. The temporal shaping of the UV laser pulse is achieved using a set of α-BBO crystals,

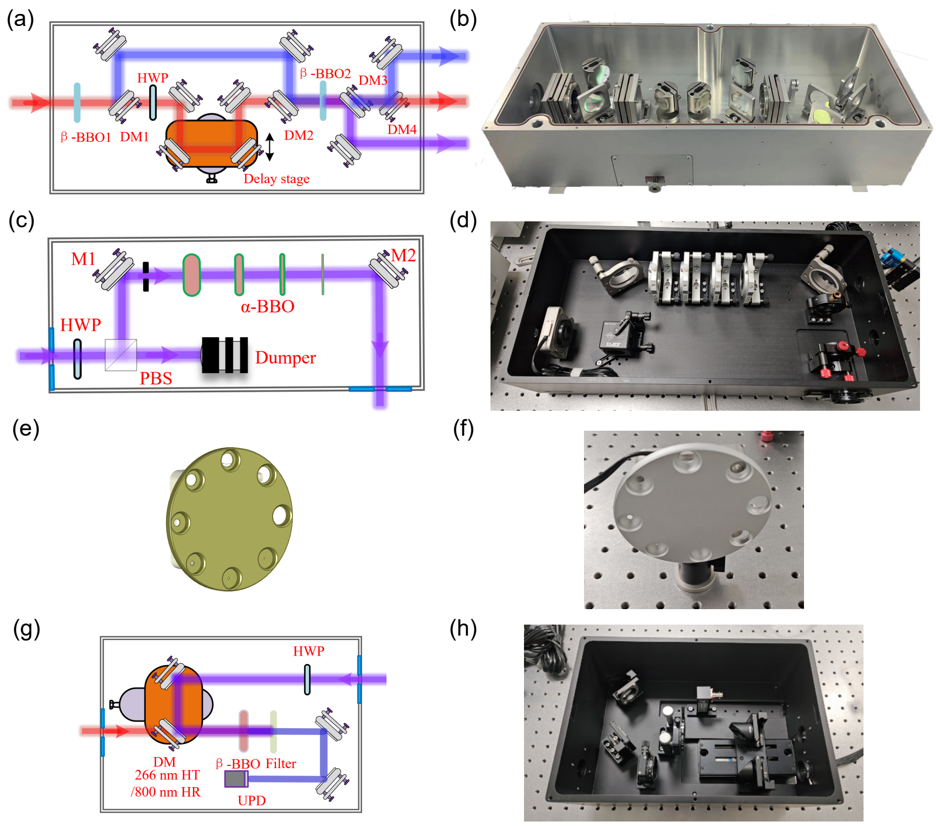

Fig. 2. The optical design schematics and assembled setups of photocathode drive laser system. (a)-(b) the third-harmonic generation , (c)-(d) the energy tuner and pulse shaping modular, (e)-(f) the iris aperture, (g)-(h) the UV-IR cross-correlation. β-BBO: Barium Borate; HWP: Half-wave plate; DM: dichroic mirror; PBS: Glan laser polarizing prism; UPD: ultrafast photodetectors.

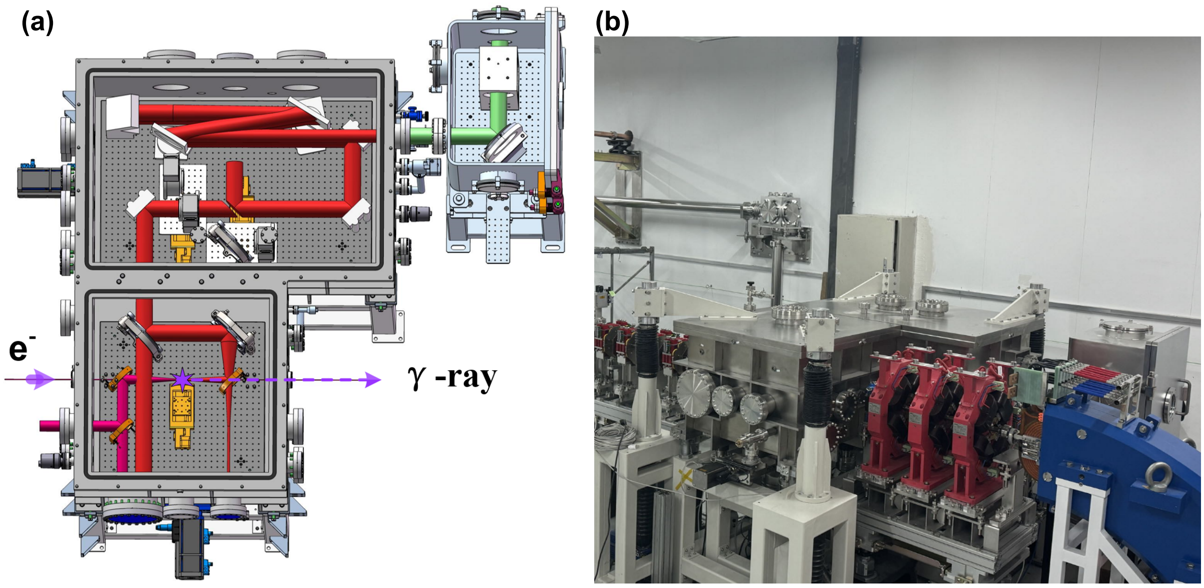

Fig. 3. The scheme designs (a) and assembled setup (b) of the ICS laser system without laser amplifier.

which will be detailed in the next chapter. A transversely truncated Gaussian laser with a beam size of 0.2-2 mm is produced by 8 iris apertures fixed on a motorized rotation mount, as shown in Fig. 2(e)-(f). A UV-IR cross-correlation setup is used to measure UV laser temporal distribution, as shown in c(g)-(h), the measurement range is 50 fs $\sim$ 300 ps.

The THG and fundamental laser generate SH laser through difference-frequency generation (β-BBO, 0.1 mm-thickness, $\theta = 44.3°$). By scanning the time delay and measuring the intensity variation of the SH laser, the temporal profile of the TH laser is obtained.

Figure 3(a) shows the layout of the ICS laser system. The vacuum ICS chamber adopts an L-shaped design scheme. First, an ultra-shot laser with pulse durations ranging from 100 fs to 10 ps is produced by the compressor. Then, the laser frequency is doubled using a 0.59-mm-thick type-I KDP crystal[32]. In the design, the positions of the SHG crystal and the dichroic mirror can be motorized to adjust the laser wavelength for generating γ-rays with different energies. The modulated laser is focused by an off-axis parabolic mirror (OAP) with a 400 mm focal length and collides with the electron beam. The focus size is <10 μm (RMS), and the beam pointing stability over time is < 2 μrad. Ultimately, the residual laser exits the vacuum chamber through a perforated OAP and a mirror to a dump. A very small portion of the laser transmitted through the back of the mirror will be used for monitoring of the ICS laser pointing position and focal intensity distribution.As shown in Fig.3(b), the vacuum ICS chamber has been installed on the beamline, and the transmission optical components inside the chamber will be setup in recently.

III. RESULTS AND DISCUSSION

A. Photo Injector Driving Laser

Figure 4 shows the THG results with a Ti:sapphire laser system delivering 8.2 mJ pulses with 33 fs duration and a 40 nm bandwidth. Two type-I β-BBO crystals were used for SHG and THG, respectively. As shown in Fig. 4(a), the UV pulse energy over 4 hours is 1.98 mJ, with a jitter (RMS) of 0.56%, and the THG conversion efficiency is 24%. The temporal shape of the UV pulse measured by the UV-IR cross-correlation (Fig. 2(d)), is depicted in Fig. 4(b) with a pulse duration of 155 fs (FWHM). In the experiment, the fundamental laser has a bandwidth of 40 nm. As the laser pulse travels through the material, it broadens due to the different group velocities of its frequency components in the crystal. Furthermore, the group velocity difference between the fundamental and SH laser in the crystal causes the two beams to separate spatially, leading to an increase in the pulse width. This effect is particularly noticeable in sum-frequency generation. Figure 4(c) illustrates the spectrum of UV pulse, centered at 267 nm with a bandwidth of 1.7 nm (FWHM).

An optical pulse shaping technique based on birefringent α-BBO crystals is employed to generate a flat-top UV laser pulse with picosecond duration[27]. The schematic diagram of the pulse shaper is shown in Fig. 5(a), where a linearly polarized laser pulse sequentially passes through four α-BBO crystals with thickness of L=4.72 mm, 2.36 mm, 1.18 mm, and 0.59 mm. The ordinary axis of the first and third crystals is oriented at 45° to the input pulse polarization direction, while the ordinary axis of the second and fourth crystals is

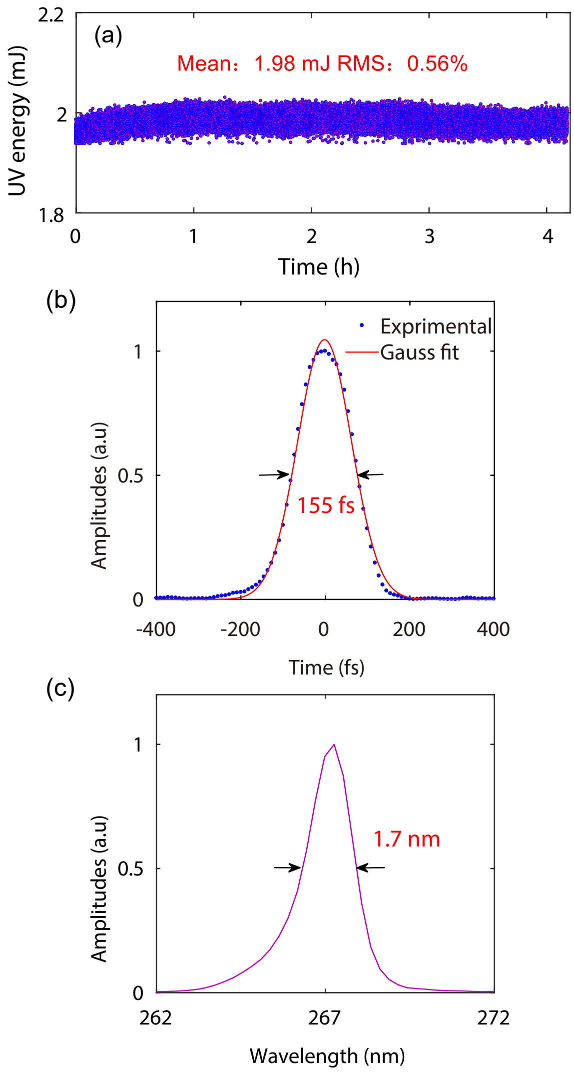

Fig. 4. The UV laser parameters output of the THG converter. (a) pulse energy over 4 hours, (b) temporal shape of experimental (blue dote) and Gauss fit (red line), (c) spectrum.

parallel to that direction. Therefore, the polarization of the 16 generated pulses is perpendicular to each other for adjacent pulses. The time delay between each adjacent pulse is 0.45 ps, which can be calculated by Equation 1 below.

$$\Delta\tau = L \cdot [n_o(\lambda_0) - n_e(\lambda_0)]/c, \tag{1}$$

where L= 0.59 mm is the thickness of the α-BBO crystal,$n_o(\lambda_0) \approx 2.02$, $n_e(\lambda_0) \approx 1.79$ are the group velocity refractive indices of the ordinary and extraordinary axes[33], and c is the speed of light in vacuum.

Figure 5(b) shows the calculation results of pulse stacking by sixteen Gaussian pulses with a 0.55 ps (FWHM) pulse duration, and a pulse spacing of 0.45 ps. The shaped pulse has a flat-top distribution with a pulse duration of 7.2 ps (FWHM). The pulse rising and falling time (10%-90%) is 0.48 ps, and the peak-to-valley ripple in the flat-

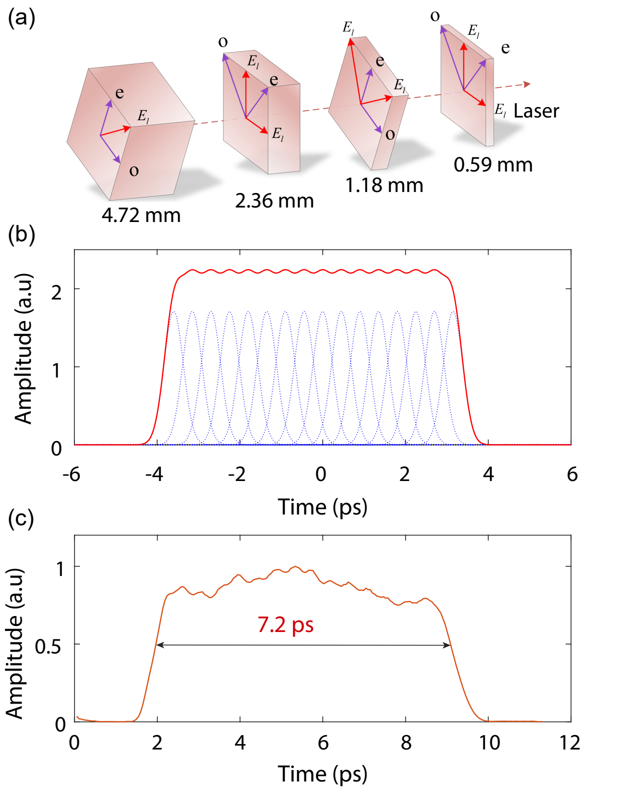

Fig. 5. The UV laser pulse shaping. (a) Schematic of α-BBO crystal serials, (b) the calculation results of pulse stacking by sixteen Gaussian pulses (c) the temporal profile of shaped UV pulse.

top region is 2%. In the experiment, due to the group delay dispersion (GDD) induced by the α-BBO crystals (8.85 mm-thickness, GDD:4528.70 fs^2), Glan polarizing prism (25.4 mm-thickness, GDD:4977.35 fs^2), lens (16 mm-thickness, GDD:3135.34 fs^2), windows (12 mm-thickness, GDD:2351.50 fs^2) and air (18 m, GDD:1811.69 fs^2) during the laser transmission, the duration of the single UV pulse broadens to approximately 0.55 ps (FWHM). The pulse duration measured in the experiment is greater than the calculated value of 0.34 ps, which was determined based on the GDD of the dispersive medium. This discrepancy might be due to the initial chirp in the UV laser pulses produced at the THG output. As shown in Fig 4(c), the UV laser spectral bandwidth is 1.7 nm, corresponding to a Fourier transform-limited pulse duration of 62.69 fs. The shaped flat-top UV pulse temporal profile is shown in Fig. 5(c), with a 7.2 ps (FWHM) pulse duration, which is in agreement with the calculation results. However, the pulse rising and falling time (10%-90%) is 0.62 ps and 0.86 ps, and the peak-to-valley ripple in the flat-top region is 20% in the experimental. This might be attributed to the discrepancies in the angular rotation of the crystal α-BBO crystals and the distribution of the single UV laser pulses.

The spatial shaping of the laser distribution on the photocathode is achieved using a method that combines aperture truncation and image relay. The UV pulse travels from the laser room to the photocathode over a total distance of about 18 m. Initially, we simulated the optical transportation in the laser room because the accelerator beamline had not yet been completed. The laser profile on the aperture is imaged onto the photocathode gun by a two-stage cascaded image relay system with a demagnification 6:1 (f1=3m, f2=1.5m, f3=3m, f4=1m). Figure 6(a) displays the transverse distribution of four UV laser beams of varying sizes on the photocathode, achieving high quality truncated Gaussian or flat-top transverse beam shape. The UV pulses energy on the photocathode and the transmission efficiency depending on the output energy after the energy tuner with different beam sizes are shown in Fig. 6(b) and Fig. 6(c), respectively. The maximum UV laser pulse energy is 0.58 mJ with a beam size of 2 mm. The transmission efficiency decreases with increasing input laser energy due to two-photon absorption in the α-BBO crystals, where higher intensity results in greater absorption. Under conditions of large beam size and low pulse energy, the transmission efficiency maximizes at 56%.

Based on the experimental results of the spatial-temporal distribution of the driving laser (5(b) and 6(a)-1.3 mm), we performed electron beam dynamics simulations of the VIGAS at a charge of 200 pC using GPT code. In the simulation, the normalized rms emittance of the electron beams are presented in 7, where the z-axis represents the beam transport position. The blue dashed line and the orange solid line represent the simulation results using the ideal flat-top distribution and the experimental results, respectively. As shown in the figure, at z = 14 m, the normalized rms emittance for the ideal laser and experimental result simulations is 0.33 mm·mrad and 0.60 mm·mrad, respectively. This variance is attributed to the inhomogeneity in the spatial-temporal distribution of the driving laser. The fluctuations in the spatial-temporal distribution of the driving laser result in increased nonlinear space charge forces, leading to amplified beam divergence and higher transverse emittance[34].

B. ICS Laser System

The present output parameters of the ICS laser in the laser room are shown in Fig. 8. Figure 8(a) illustrates the compressed laser pulse energy of 3.34 J with a pulse-to-pulse jitter of 0.5%(RMS) over 8 hours. Figure 8(b) shows the transverse distribution of laser beams at the near-field, $\sim$65 mm($1/e^2$) in the horizontal, and $\sim$63 mm($1/e^2$) in the vertical directions. The temporal distribution and spectrum of the laser pulse after compression are shown in Fig. 8(c)-(d), with a duration of 103 fs (FWHM), and a spectral bandwidth of 12 nm (FWHM). Figure 8(e)-(f) depicts the RMS pointing stability of the focal point of an 800 nm laser after being focused by a lens with 1000 mm focal length, which is 1.48 μrad for horizontal and 1.94 μrad for vertical direction.

In the ICS process between relativistic electron beams and ultra-short laser pulses, using shorter wavelength lasers can produce higher X/γ-rays photon energy. Therefore, we have experimentally studied the SHG of the ICS laser (Fig.8) with a KDP crystal. To achieve a high-quality focal distribution of the 400 nm laser, we used a thin KDP crystal (0.59 mm-

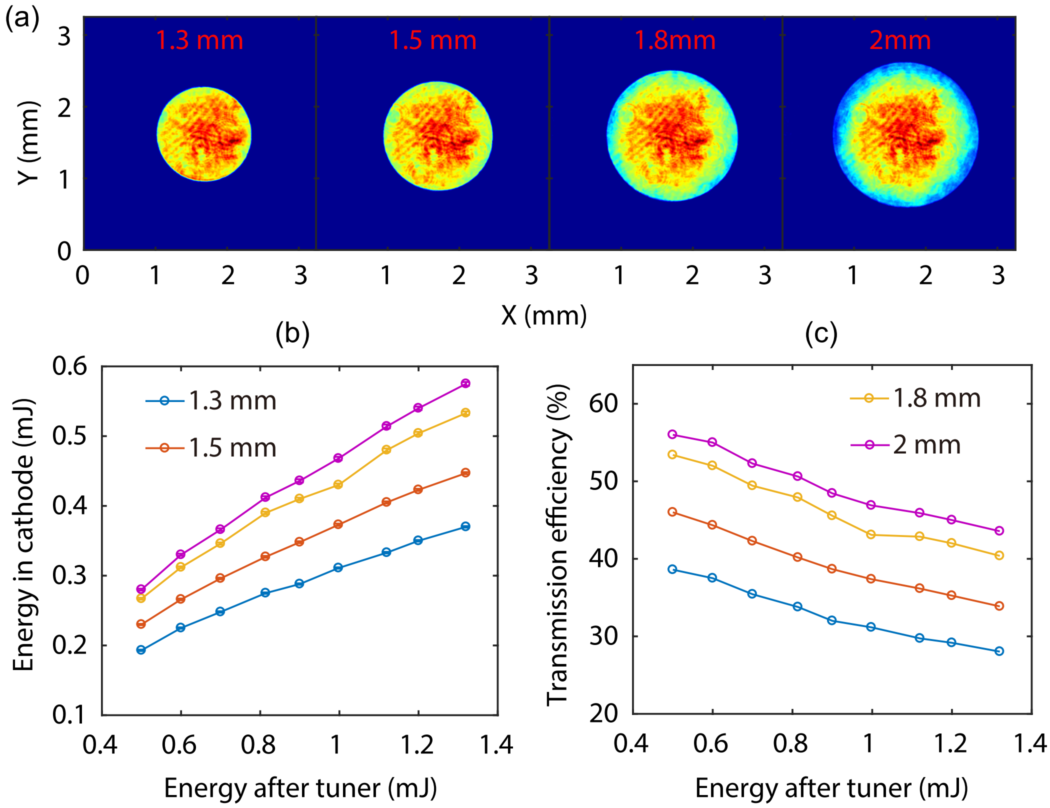

Fig. 6. The UV beam profile and transmission. (a) The UV beam profile on the photocathode. (b)- (c) The UV pulse energy and transmission efficiency versus input pulse energy for four beam sizes.

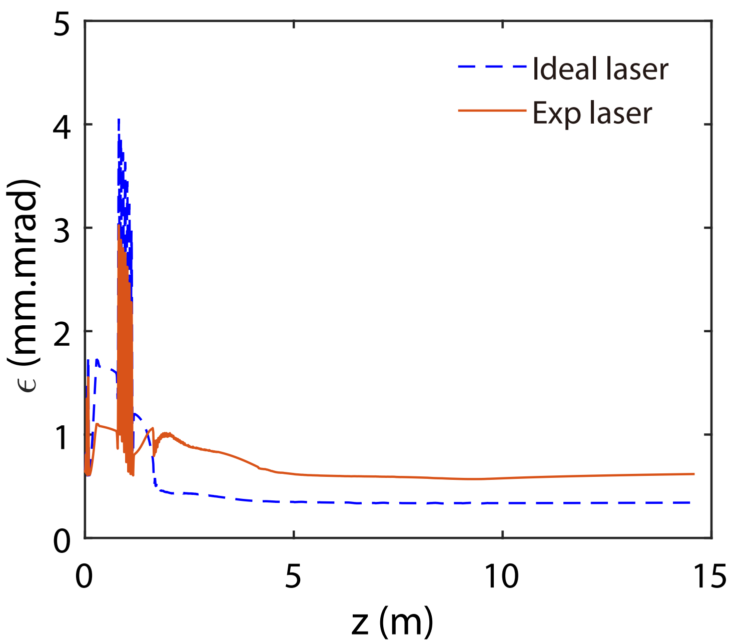

Fig. 7. The beam normalized rms emittance simulated by GPT code based on the ideal flat-top distribution (blue dashed line) and the experimental results (orange solid line) of the driving laser.

thickness, 75 mm-diameter, $\theta = 44.9°$, ϕ=45°) for SHG in the initial phase of the experiment. Figure 9(a) shows the

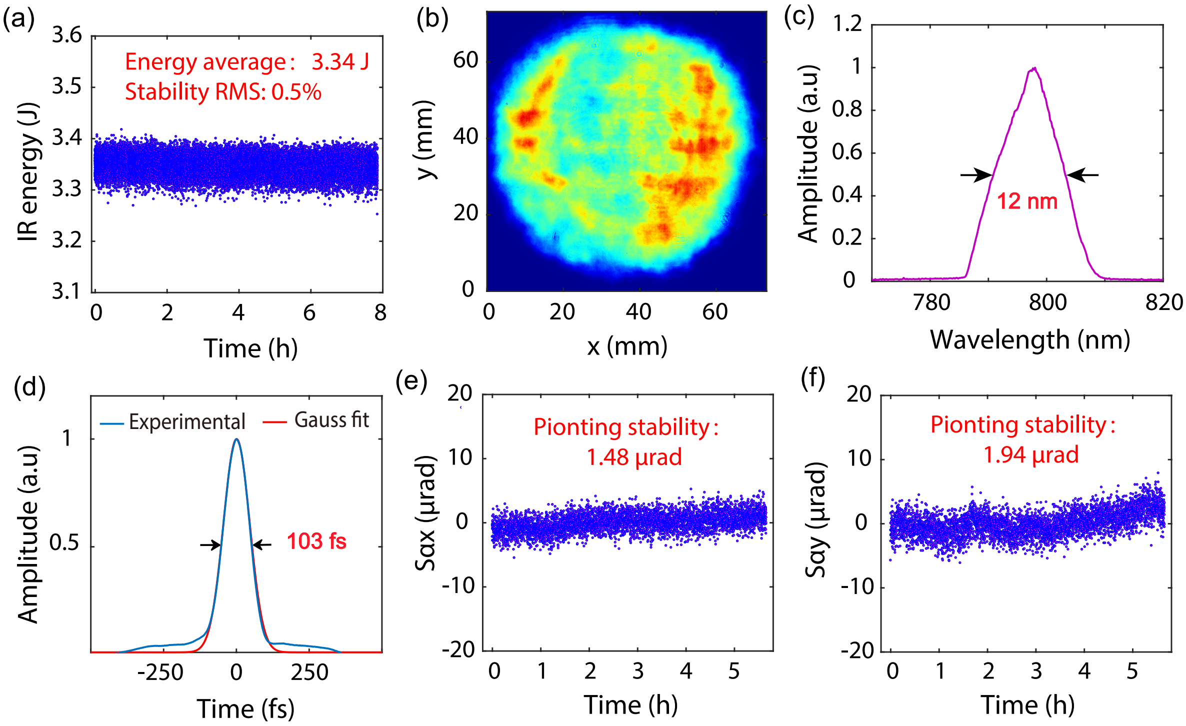

Fig. 8. The output parameters of the ICS laser. (a) Pulse energy and stability over 8 hours, (b) laser beam transverse distribution at the near-field, (c) spectrum, (d) temporal distribution, (e)-(f) the pointing stability over 5 hours.

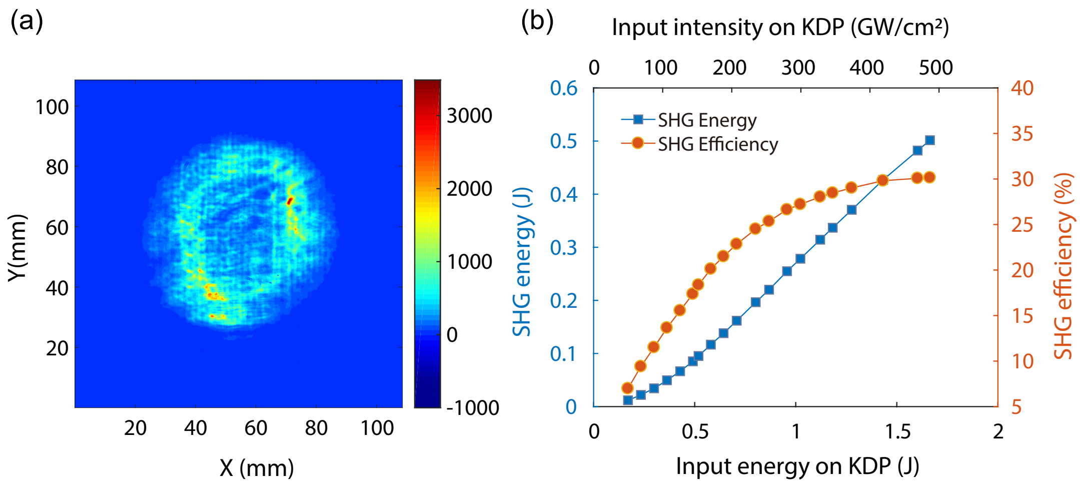

Fig. 9. The parameters of SHG. (a) The transverse distribution of the SHG laser beams, (b) SHG pulse energy and conversion efficiency in dependence of the incident fundamental pulse energy and intensity on the KDP crystal.

transverse distribution of the SHG laser beams by an input fundamental intensity of ~50 GW/cm^2. The diameter in x direction (horizontal) and y directions (vertical) are ~65 mm and ~62 mm (full width at $1/e^2$), respectively. Measurements of the SHG pulse energy and conversion efficiency as functions of 800 nm laser energy and intensity on the KDP are shown in Fig. 9(b). At lower input laser intensities, the SHG energy is proportional to the square of the input laser intensity. Nevertheless, with further increasing of the input intensity, the SHG conversion efficiency begins to saturate due to the effects of group-velocity mismatch and Kerr nonlinearities[31, 35, 36]. At the maximum pump energy of 1.6 J (~500 GW/cm^2) on the KDP crystal, we measured a 0.5 J SHG pulse energy and obtained a 30 % conversion efficiency.

The laser focal intensity distribution is a key factor influ-

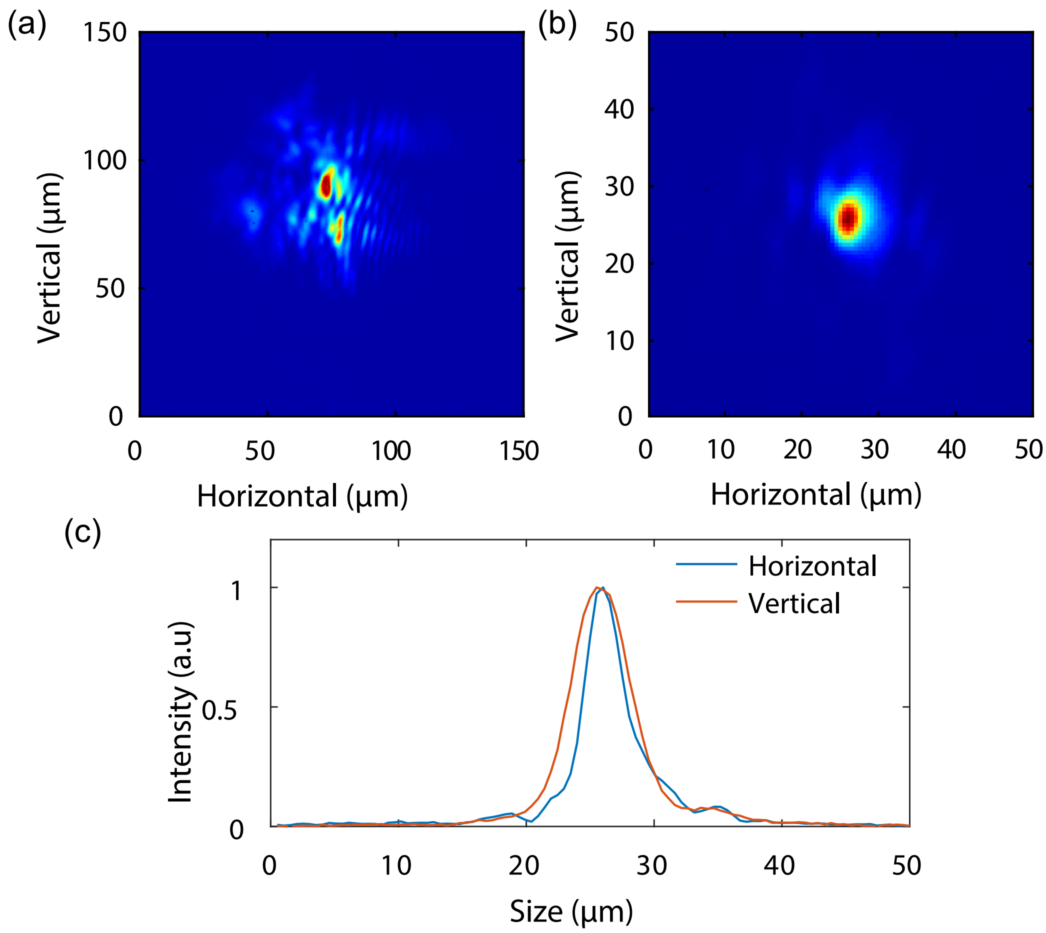

Fig. 10. The SH laser focal intensity distribution. (a) Without wave-front correction, (b) with wave-front correction, (c) cross-section intensity profiles of (b).

encing the photon yield of X/γ-rays in the ICS process[28]. However, significant wavefront distortions of the SH laser are induced by nonlinear effects during the frequency doubling process, making it challenging to achieve a good focal intensity distribution[37, 38]. In this paper, we use a wavefront sensor (PHASICS, SID4-GE) and a deformable mirror (DYNAMIC OPTICS, DM6490) to correct the wavefront of the SH laser pulse. The wavefront sensor measures the focus beam wavefront through a lens telescope, and generates an error signal which is the distance to a flat wavefront. An adaptive optics loop software was used to convert the wavefront error signal into commands that control the deformable mirror shaping the wavefront. The loop is closed so that it can react to any change in the laser beam wavefront, and the feedback progress between the sensor and deformable mirror goes on until a steady state is obtained. Figure 10 shows the SH laser focal intensity distribution without and with wavefront correction for an input fundamental intensity of $\sim$50 GW/cm^2. As shown in Fig. 10(a), the SH laser focal intensity distribution without wavefront correction exhibits abundant low-intensity spatial wings due to nonlinear effects in the KDP crystal. By employing a deformable mirror, the wavefront aberration was corrected from 3.8λ to 0.5λ peak-to-valley. The SH focal intensity distribution with wavefront correction and its cross-section intensity profiles are depicted in Fig. 10(b) and Fig. 10(c), respectively. The horizontal and vertical beam diameters are 7.4 μm$(1/e^2)$ and 9.2 μm $(1/e^2)$, with corresponding peak-to-average ratios of 2.1 and 1.7, respectively.

To achieve a higher SH energy and conversion efficiency required for the VIGAS project, a thicker KDP crystal will be used in the second phase of the experiment. Simultaneously, we will investigate the effect of different crystal thicknesses on the SH laser focal intensity distribution, which is of great significance for laser-matter interaction experiments.

IV. CONCLUSION

In this paper, we present the photo-injector driving laser system and ICS laser system for the VIGAS facility, currently under commission at Tsinghua University. The engineering modular design improves the stability and flexibility of the laser system. We achieve a flat-top temporal-spatial

distribution UV pulses with 7.2 ps (FWHM) pulse duration and 0.2-2mm beam diameters through pulse shaping, facilitating high-quality electron bunch generation. Through the beam dynamics simulation of GPT, a election beam with a normalized rms emittance of 0.60 mm·mrad at 200 pC was obtained for the spatial-temporal shaped driving laser.The photo-injector drive laser with maximum pulse energy of 0.58 mJ and transportation efficiency of 56%, can ensure the beam charge to reach nC level.

Meanwhile, we described the ICS scattering laser with two alternative central wavelength of 800 nm and 400 nm to generate γ-ray with different energy regions. The SHG and focusing characteristics based on ultra-intense femtosecond laser pulses with a 0.59-mm thickness KDP crystal are analyzed. Experimentally, an intense SH laser pulse with 0.5 J pulse energy and a desirable focal intensity distribution are obtained.

Author contributions All the authors contributed to the conception and design of the study. Material preparation, data collection, and analysis were performed by Qi-li Tian, Qiang Gao, Xing Liu, and Li-xin Yan. The first draft of the manuscript was written by Qi-li Tian, and all the authors commented on the previous versions of the manuscript. All authors have read and approved the final manuscript.

Data availability The data that support the fndings of this study are openly available in Science Data Bank at https://cstr.cn/31253.11.sciencedb.j00186.00368 and https://www.doi.org/10.57760/sciencedb.j00186.00368

DECLARATIONS

The authors declare that they have no known competing financial interests or personal relationships that could have appeared to influence the work reported in this paper.

REFERENCE

[1] T. Hayakawa, T. Shizuma, T. Miyamoto, *et al.*, Spatial anisotropy of neutrons emitted from the $^{56}\mathrm{Fe}(\gamma, n)^{55}\mathrm{Fe}$ reaction with a linearly polarized γ-ray beam. Phys. Rev. C. **93**: 044313 (2016). DOI:10.1103/PhysRevC.93.044313

[2] J. Lin, H.Z. Zhang, Z. Zhang, *et al.*, Simulation Study on Pinhole Imaging of $^{239}\mathrm{Pu}$ Using Nuclear Resonance Fluorescence With Laser Compton Scattering Gamma Rays. IEEE Transactions on Nuclear Science, **71**: 2045-2055 (2024). DOI:10.1109/TNS.2024.3439624

[3] B. Günther, R. Gradl, C. Jud, *et al*, The versatile X-ray beamline of the Munich Compact Light Source: design, instrumentation and applications. J. Synchrotron Rad. **27**: 1395-1414 (2020). DOI:10.1107/S1600577520008309

[4] S. Kulpe , M. Dierolf, B. Günther, *et al.*, Dynamic K-edge subtraction fluoroscopy at a compact inverse-Compton synchrotron X-ray source. Sci. Reports. **10**: 9612 (2020). DOI:10.1038/s41598-020-66414-x

[5] R. Gradl, M. Dierolf, L. Yang, *et al.*, Visualizing treatment delivery and deposition in mouse lungs using in vivo x-ray imaging. Journal of Controlled Release. **307**: 282-291 (2019). DOI:10.1016/j.jconrel.2019.06.035

[6] Z. Chi, L. Yan, Y. Du, *et al.*, Recent progress of phase-contrast imaging at Tsinghua Thomson-scattering X-ray source. Nucl. Instrum. Methods Phys. Res., Sect. B. **402**: 364–369 (2017). DOI:https://doi.org/10.1016/j.nimb.2017.02.062

[7] Z. Chi, Y. Du, W. Huang, *et al.*, Linearly polarized X-ray fluorescence computed tomography based on a Thomson scattering light source: a Monte Carlo study. J. Synchrotron Rad. **27**: 737–745 (2020). DOI:10.1107/S1600577520003574

[8] Z. Chi, H. Zhang, J. Lin, *et al.*, Simultaneous fluorescence and Compton scattering computed tomography based on linear polarization X-ray. Nucl. Sci. Tech. **35**: 170 (2024). DOI:10.1007/s41365-024-01525-y

[9] C. Vaccarezza, D. Alesini, M.P. Anania, *et al.*, The SPARC_LAB Thomson source. Nucl. Instrum. Methods Phys. Res. Sect. A. **829**: 237-242 (2016). DOI:10.1016/j.nima.2016.01.089

[10] M. Jacquet, P. Alexandre, M. Alkadi, *et al.*,First production of X-rays at the ThomX high-intensity Compton source. Eur. Phys. J. Plus. **139**: 1-11 (2024). 10.1140/epjp/s13360-024-05186-z

[11] D. Habs, T. Tajima, V. Zamfir, *et al.*, Extreme light infrastructure–nuclear physics (ELI–NP): new horizons for photon physics in Europe. Nuclear Physics News. **21**: 23-29 (2011). DOI:10.1080/10619127.2010.529741

[12] S. Amano, K. Horikawa, K. Ishihara, *et al.*, Several-MeV γ-ray generation at NewSUBARU by laser Compton backscattering. Nucl. Instrum. Methods Phys. Res. Sect. B. **602**: 337-341 (2009). DOI:10.1016/j.nima.2009.01.010

[13] F. Albert, S.G. Anderson, D.J. Gibson, *et al.*,Characterization and applications of a tunable, laser-based, MeV-class Compton-scattering γ-ray source. Phys. Rev. ST Accel. Beams, **13**: 070704 (2010). DOI:10.1103/PhysRevSTAB.13.070704

[14] W. Guo, W. Xu, J.G. Chen, *et al.*, A high intensity beam line of γ-ray up to 22 MeV energy based on Compton backscattering. Nucl. Instrum. Methods Phys. Res. Sect. A. **578**: 457-462 (2007). DOI:10.1016/j.nima.2007.05.322

[15] H. Wang, G. Fan, L. Liu, *et al.*, Commissioning of laser electron gamma beamline SLEGS at SSRF. Nucl. Sci. Tech. **33**: 87 (2022). DOI:10.1007/s41365-022-01076-0

[16] L.X. Liu, H.W. Wang, G.T. Fan, *et al.* The SLEGS beamline of SSRF. Nucl. Sci. Tech. **35**: 111 (2024). DOI:10.1007/s41365-024-01469-3

[17] G.P. An, Y.L. Chi, Y.L. Dang, *et al.*, High energy and high brightness laser compton backscattering gamma-ray source at IHEP. Matter Radiat. Extremes, **3**: 219-226 (2018). DOI:10.1016/j.mre.2018.01.005

[18] H. Chen, L.X. Yan, Q.L Tian, *et al.*, Commissioning the photoinjector of a gamma-ray light source.Phys. Rev. ST Accel. Beams. **22**: 053403 (2019). DOI:10.1103/PhysRevAccelBeams.22.053403

[19] Y. Du, L. Yan, J. Hua, *et al.*, Generation of first hard X-ray pulse at Tsinghua Thomson Scattering X-ray Source. Rev. Sci. Instrum. **84**: 053301 (2013). DOI:10.1063/1.4803671

[20] C. Tang, W. Huang, R. Li, *et al*.,Tsinghua Thomson scattering X-ray source. Nucl. Instrum. Methods Phys. Res. Sect. B. **608**: S70-S74 (2009). DOI:10.1016/j.nima.2009.05.088
[21] Y. Du, H. Chen, H. Zhang, *et al*., A very compact inverse Compton scattering gamma-ray source. High Power Laser Part.Beams. **34**: 104010 (2022). DOI:10.11884/HPLPB202234.220132
[22] L. Winkelmann, A. Choudhuri, H. Chu, *et al*.,The European XFEL photocathode laser. 39th Free Electron Laser Conference, **21**: 423-426 (2019). DOI:10.18429/JACoW-FEL2019-WEP046
[23] M.P. Minitti, J.S. Robinson, R.N. Coffee, *et al*., Optical laser systems at the linac coherent light source. J. Synchrotron Rad, **22**: 526–531 (2015). DOI:10.1107/S1600577515006244
[24] W.H. Wang, C. Li, Z.G. He, *et al*. Commissioning the photocathode radio frequency gun: a candidate electron source for Hefei Advanced Light Facility. Nucl. Sci. Tech. **33**: 23 (2022). DOI:10.1007/s41365-022-01000-6
[25] L.M. Zheng, Y.C Du, Z. Zhang, *et al*.,Development of S-band photocathode RF guns at Tsinghua University. Nucl. Instrum. Methods Phys. Res. Sect. A. **834**: 98-107 (2016). DOI:10.1016/j.nima.2016.07.015
[26] I.V. Bazarov, D.G. Ouzounov, B.M. Dunham, *et al*., Efficient temporal shaping of electron distributions for high-brightness photoemission electron guns. Phys. Rev. ST Accel. Beams. **11**: 040702 (2008). DOI:10.1103/PhysRevSTAB.11.040702
[27] L. Yan, J. Hua, Y. Du, *et al*.,UV pulse trains by α-BBO crystal stacking for the production of THz-rap-rate electron bunches. Nucl. Instrum. Methods Phys. Res. Sect. B. **608**: S70-S74 (2009). DOI:10.1017/S0022377812000281
[28] C. Sun, Y.K. Wu, *et al*., Theoretical and simulation studies of characteristics of a Compton light source. Phys. Rev. ST Accel. Beams. **14**:044701 (2011). DOI:10.1103/PhysRevSTAB.14.044701
[29] C. Lin, H. Zha, J. Shi, *et al*., Design, fabrication, and testing of low-group-velocity S-band traveling-wave accelerating structure. Nucl. Sci. Tech. **33**: 147 (2022). DOI:10.1007/s41365-022-01124-9
[30] C. Lin, H. Zha, J. Shi, *et al*., Fabrication, tuning, and high-gradient testing of an X-band traveling-wave accelerating structure for VIGAS. Nucl. Sci. Tech. **33**: 102 (2022). DOI:10.1007/s41365-022-01086-y
[31] Q. Gao, H. Zha, J.R. Shi, *et al*., Design and test of an X-band constant gradient structure. Phys. Rev. Accel. Beams. **27**: 090401 (2024). 10.1103/PhysRevAccelBeams.27.090401
[32] C. Aparajit, K. Jana, AD Lad, *et al*., Efficient second-harmonic generation of a high-energy, femtosecond laser pulse in a lithium triborate crystal. Opt. Lett., **46**: 3540–3543 (2021). DOI:10.1364/OL.423725
[33] G. Tamošauskas, G. Beresnevičius, D. Gadonas, *et al*., Transmittance and phase matching of BBO crystal in the 3um-5um range and its application for the characterization of mid-infrared laser pulses. Opt. Mater. Express, **8**: 1410-1418 (2018). DOI:10.1364/OME.8.001410
[34] J. Yang, F. Sakai, T. Yanagida, *et al*., Low-emittance electron-beam generation with laser pulse shaping in photocathode radio-frequency gun. J. Appl. Phys, **92**: 1608–1612 (2002). DOI:10.1063/1.1487457
[35] I.A. Begishev, M. Kalashnikov, V. Karpov, *et al*., Limitation of second-harmonic generation of femtosecond Ti:sapphire laser pulses. J. Opt. Soc. Am. B., **21**: 318-322 (2004). DOI:10.1364/JOSAB.21.000318
[36] T. Ditmire, A. M. Rubenchik, D. Eimerl, *et al*.,Effects of cubic nonlinearity on frequency doubling of high-power laser pulses. J. Opt. Soc. Am. B. **13**:649–655 (1996). DOI:10.1364/JOSAB.13.000649
[37] J. Queneuille, F. Druon, A. Maksimchuk, *et al*, Second-harmonic generation and wave-front correction of a terawatt laser system. Opt. Lett., **25**: 508–510 (2000). DOI:10.1364/OL.25.000508
[38] A. Marcinkevičius, R. Tommasini, G.D. Tsakiris, *et al*.,Frequency doubling of multi-terawatt femtosecond pulses. Applied Physics B, **79**: 547–554 (2004). DOI:10.1007/s00340-004-1612-5